Chemical Science

ROYAL SOCIETY OF CHEMISTRY

EDGE ARTICLE

View Article Online
View Journal | View Issue

Cite this: *Chem. Sci.*, 2025, **16**, 20314

All publication charges for this article have been paid for by the Royal Society of Chemistry

Dual-functional photoredox catalytic thiocyanation and hydroxylation using a donor–acceptor COF

Tamagna Mandal,†[a] Anupam Dey,†[b] Dipayan Mandal[b] and Tapas Kumar Maji *[ab]

Heterogeneous photoredox catalysis, a powerful approach for activating small molecules, is experiencing a notable resurgence due to the availability and eco-friendly benefits of natural sunlight. Most of the photoredox organic transformations are either electron or hole mediated pathways to drive the reaction with the assistance of sacrificial agents. Recently, the simultaneous use of photogenerated electrons and holes for reductive and oxidative reactions has emerged as an intriguing approach in organic photoredox reactions. In this study, we report the design and synthesis of a donor–acceptor imine based **Py-Tz** COF, composed of pyrene and tetrazine based building units and explored oxidative thiocyanation and reductive hydroxylation reactions. The efficient photogenerated electron–hole separation, driven by pyrene's strong electron-donating and tetrazine's electron-accepting properties, along with a low exciton binding energy (61.4 meV), facilitated both reactions efficiently, as realized in the transformation of substrates having different functional groups. **Py-Tz** COF was further employed as a photocatalyst for CO_2 reduction, coupled with a thiocyanation reaction within a single redox cycle. By leveraging the distinct oxidation and reduction energy levels of the **Py-Tz** COF, oxidative thiocyanation and reductive hydroxylation were achieved in a one-pot transformation. The mechanism of each reaction was evaluated by identifying the reaction intermediates through *in situ* diffuse reflectance infrared Fourier transform spectroscopy (DRIFTS), supported by the different photophysical and electron paramagnetic resonance (EPR) studies. Post-catalysis characterizations confirmed that the COF retained its crystallinity and photostability after the reactions. This report highlights the unique application of a metal-free, heterogeneous photocatalyst for two different photoredox reactions conducted in a single pot.

Received 21st April 2025
Accepted 15th September 2025

DOI: 10.1039/d5sc02909k

rsc.li/chemical-science

Introduction

Owing to its sustainable, recyclable, and versatile methodology, heterogeneous photoredox catalysis has undergone a thriving renaissance in recent times.[1] A traditional semiconductor-based photoredox catalysis process consists of four common steps: (i) visible light absorption, (ii) generation of charge carriers, (iii) migration of the charge carriers to the surface of the catalyst, and finally, (iv) participation in the redox reactions.[2] The reduction processes are propelled by the photogenerated electrons (e^-), whereas the oxidation process is carried out independently by the holes (h^+).[3,4] Nevertheless, the majority of photocatalytic systems fail to fully capitalize on the economic advantages of the photogenerated charges. Typically, only either e^- or h^+ is utilized in a single photoredox reaction, resulting in the production of solely reduction or oxidation products. Moreover, a sacrificial reagent, either electron donor or acceptor, has typically been added to the reaction medium in order to stop the recombination process and accelerate the reaction kinetics.[5,6] The use of these sacrificial agents not only increases the operational cost but also leads to waste formation, hindering the achievement of the full potential of the overall photoredox system. Thus, to address this limitation, a dual-functionalized photocatalytic system has been developed that can effectively utilize both e^- and h^+ to generate simultaneously two different value-added products without incurring additional costs or waste.[7,8] Regarding this, various strategies have been proposed in the literature, including doping in semiconductors, metal nanoparticles supported on semiconductors, and the construction of two semiconductor-based heterojunctions. However, metal-free organic semiconductor-based dual-functional, heterogeneous photocatalytic redox systems are yet to be explored.[9–13]

Covalent organic frameworks (COFs), a class of porous crystalline organic polymers, emerge as excellent catalysts for metal-free heterogeneous organic transformation reactions. The

[a]*New Chemistry Unit (NCU), School of Advanced Materials (SAMat), Jawaharlal Nehru Centre for Advanced Scientific Research, Jakkur, Bangalore 560064, India*

[b]*Chemistry and Physics of Materials Unit (CPMU), School of Advanced Materials (SAMat), Jawaharlal Nehru Centre for Advanced Scientific Research, Jakkur, Bangalore 560064, India. E-mail: tmaji@jncasr.ac.in; Web: https://www.jncasr.ac.in/faculty/*

† Contributed equally.

development of COFs in photocatalytic organic transformations is stimulated by several advantages related to the robust π-conjugated covalent framework, large surface area, and tunable band gap based on a variety of organic chromophoric building units.[14] Various types of heterogeneous photocatalytic organic transformations, like C–H functionalization,[15] sulfoxidation,[16] amine oxidation,[17] C–H borylation,[18] thioamide cyclization,[19] and alcohol oxidation[20] have been reported earlier. However, creating a robust metal-free photocatalyst that can concurrently generate and utilize electron–hole pairs while minimizing coulombic recombination remains a significant challenge. The majority of COF-based photoredox studies have reported dual-catalysis where photoexcited electrons are employed for H_2O_2 generation, while photogenerated holes participate in oxidative organic transformations. These systems are typically focused on single organic transformations mediated by reactive oxygen species (ROS), with O_2 to H_2O_2 conversion occurring as a side or supportive process. Thus, metal-free polymer-based photocatalysts reported so far have demonstrated either oxidative or reductive processes individually, but not concurrently for two distinct, synthetically valuable organic transformations.[21–24] In this regard, the construction of donor–acceptor (D–A) based COFs with low exciton binding energy is very crucial to establish the dual-functionalized photocatalytic system.[25,26] The donor–acceptor dyad in COFs facilitates the separation and migration of charge carriers *via* the intramolecular charge transfer (ICT) process, which can enhance the scope to utilize both the e^- and h^+ separately for two different redox reactions.[27]

In this context, we have synthesized a D–A based, **Py-Tz** COF with low exciton binding energy (61.5 meV) from a donor-pyrene-aldehyde [$Py(CHO)_4$] and tetrazine-amine [$Tz(NH_2)_2$] as an acceptor moiety. The well-separated highest occupied molecular orbital (HOMO) and lowest unoccupied molecular orbital (LUMO) in **Py-Tz** COF, leading to an intramolecular charge transfer (ICT) band in the visible light, led to efficient separation of electrons (e^-) and holes (h^+) that was employed for e^- and h^+ mediated hydroxylation of boronic acids and thiocyanation reaction, respectively (Scheme 1). Both reactions investigated in this study hold significant value in the domain of organic synthesis. Phenols are widely recognized for their importance in natural products, pharmaceuticals, and polymer chemistry.[28,29] Similarly, thiocyanation, involving the formation of C–SCN bonds, provides access to organo-thiocyanates an important class of sulphur-containing compounds.[30–32] Thus, we developed a green, efficient, and atom-economical photocatalytic method for both thiocyanation and hydroxylation reactions, using a D–A type **Py-Tz** COF as the photocatalyst. To monitor the real-time progression of both reactions, we performed *in situ* DRIFTS to track various key intermediates during the catalytic process. Furthermore, to identify the reactive species generated under light irradiation, we employed EPR and steady-state photoluminescence (PL) spectroscopy, which provided deeper insights into the mechanism and reactive species involved in both the photocatalytic transformations. This photocatalysis approach works well for the quantitative transformation of various substrates, including even bulky

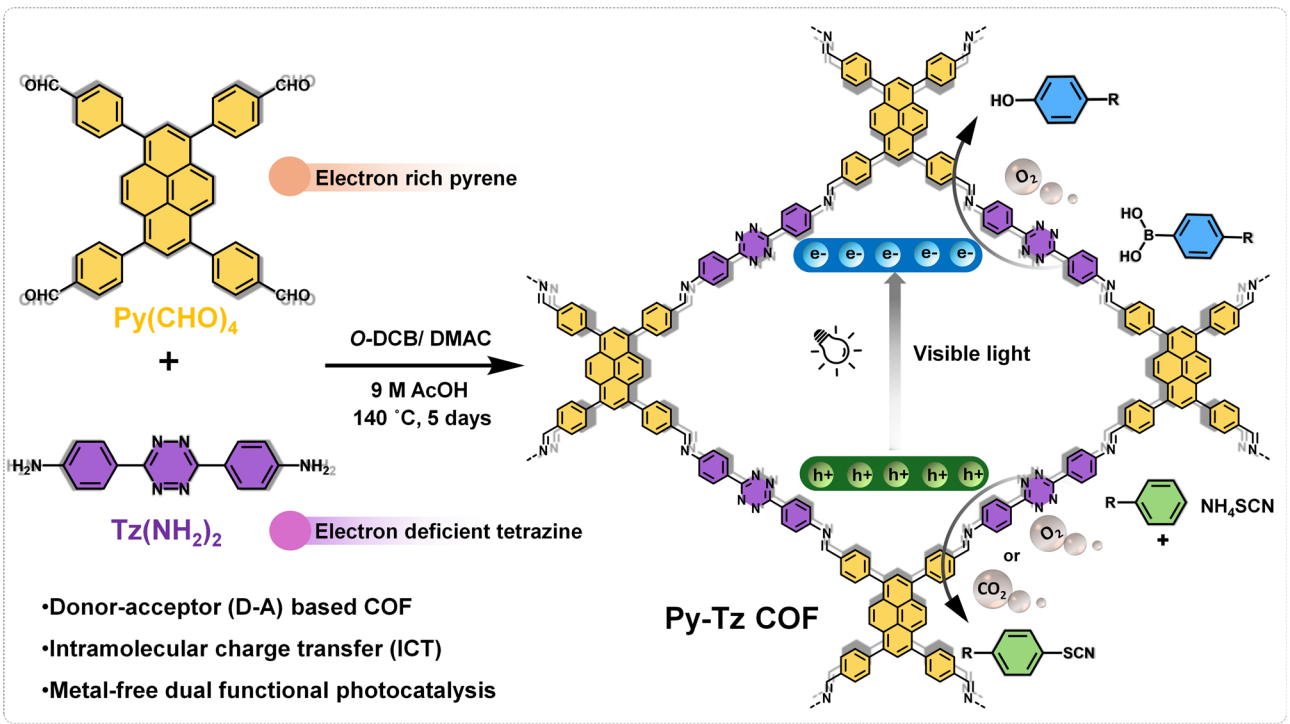

Scheme 1 Synthetic scheme of donor–acceptor **Py-Tz** COF from $Py(CHO)_4$ and $Tz(NH_2)_2$, serving as a metal-free dual-functional heterogeneous photocatalyst. Two different organic transformation reactions: e^--catalysed hydroxylation and h^+-catalysed thiocyanation reactions conducted in a single pot.

organic molecules, into the desired products. **Py-Tz** COF was also utilized to perform dual-functional photocatalytic thiocyanation and hydroxylation reactions in a single pot. Additionally, efficient dual-catalytic transformation was also achieved during simultaneous photocatalytic CO_2 to CO conversion (690.2 μmol g^{-1}) and thiocyanation reaction (≈74%). This approach presents a promising strategy for utilizing metal-free COFs in photocatalytic organic transformations while minimizing waste product formation.

Results and discussion

Py-Tz COF was synthesized from tetratopic [$Py(CHO)_4$] and ditopic tetrazine amine [$Tz(NH_2)_2$] using an imine condensation reaction by following the previous report (Scheme 1).[33] This COF was obtained as an orange fluffy solid material with a ≈75% yield (Fig. S4). The high crystalline nature of the COF was first certified by powder X-ray diffraction (PXRD) measurement. In order to acquire comprehensive structural information, COF's structure was modelled, and the PXRD pattern was simulated by considering AA and AB stacking modes (Fig. S5). For **Py-Tz** COF, the obtained experimental PXRD pattern closely matched the simulated AA stacking PXRD pattern (Fig. 1a). In the FTIR spectrum, two peaks for –C=N– stretching were observed at 1590 and 1602 cm^{-1}, which correspond to the newly formed imine bonds and tetrazine moiety, respectively (Fig. S6).[34] The ^{13}C solid-state NMR spectrum showed peaks around ~161.4 ppm and ~166.2 ppm, which were attributed to the newly formed imine carbon and tetrazine carbon, respectively (Fig. 1b).[35,36] Thermogravimetric analysis (TGA) demonstrated the thermal stability of **Py-Tz** COF up to 265 °C (Fig. S7). **Py-Tz** COF revealed a typical type-IV isotherm with a BET surface area of 1157 $m^2\ g^{-1}$ (Fig. 1c). Pore-size distribution revealed the abundance of mesopores at ~2.33 nm along with micropores at ~1.43 nm (Fig. S8). Irregular stacked-sheet morphology was realized by field emission scanning electron microscopy (FESEM) and transmission electron microscopy (TEM) (Fig. S9). AFM images also confirmed irregular-stacked 2D sheet-like morphology of the COF and the height of the sheets is within the range of ~60 nm (inset, Fig. S9c). Further, HAADF-STEM images and corresponding elemental mapping suggested a uniform distribution of C and N over **Py-Tz** COF (Fig. S10).

Solid-state UV-vis diffuse reflectance spectroscopy of **Py-Tz** COF revealed a broad absorbance in the visible range with a prominent band at ~500 nm (Fig. 2a), and the corresponding optical band gap was calculated to be 2.4 eV from the Tauc plot (inset, Fig. 2a). Time-dependent density functional theory (TDDFT) calculations considering the smallest repeating unit of the COF framework suggested that the broad absorption near 500 nm can be associated with the HOMO to LUMO transition at 483.23 nm. Further, the position of the frontier molecular orbitals of the **Py-Tz** COF was checked by the DFT method, indicating that the HOMO and LUMO were localized on the electron-rich pyrene moiety and the electron-deficient tetrazine moiety, respectively, constructing a perfect donor–acceptor framework (Fig. 2b). Thus, the absorption band corresponds to the HOMO to LUMO transition in **Py-Tz** COF, which denotes the intramolecular charge transfer (ICT) phenomenon. The additional broad band in the region 550–600 nm in the solid-state UV-vis absorption spectrum of **Py-Tz** COF could be attributed to the n–π* transition of the tetrazene moiety, as confirmed from the similar experimental band present in the solid-state UV-vis absorption spectrum of $Tz(NH_2)_2$ monomeric unit (Fig. S11).[37] TDDFT calculation also revealed a theoretical absorption band at 587.5 nm, which can be attributed to a HOMO-2 to LUMO electronic transition. Both the HOMO-2 and LUMO orbitals are localized on the tetrazine moiety, indicating that this band arises from a local excitation within the tetrazine unit (Fig. S12).

A metal-free donor–acceptor-based polymeric catalyst's efficiency strongly depends on a key parameter called Frenkel exciton binding energy (E_b),[38] which determines the Coulombic interaction and the chance of electron–hole (excitons) separation during the photocatalysis process. The **Py-Tz** COF exhibited a low exciton binding energy of 61.4 meV (Fig. S13).[39–43] The conduction band (CB) position was calculated to be −0.63 V *vs.* NHE as calculated from the Mott–Schottky measurement (Fig. S14a). Further, by adding the band gap, the valence band (VB) position was calculated to be 1.79 V *vs.* NHE (Fig. 2c). The relative band diagram of **Py-Tz** COF depicts that the CB is more

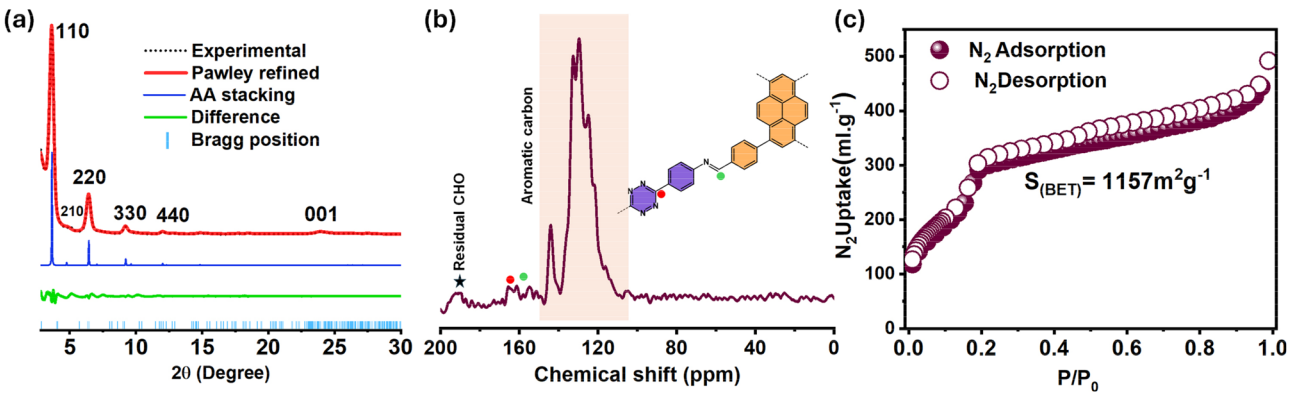

Fig. 1 (a) PXRD patterns of **Py-Tz** COF; experimental obtained (dotted black), Pawley refined (red), simulated pattern for AA stacking (blue) and their difference (green). (b) Solid-state ^{13}C NMR spectra of **Py-Tz** COF. (c) N_2 sorption isotherm of **Py-Tz** COF measured at 77 K.

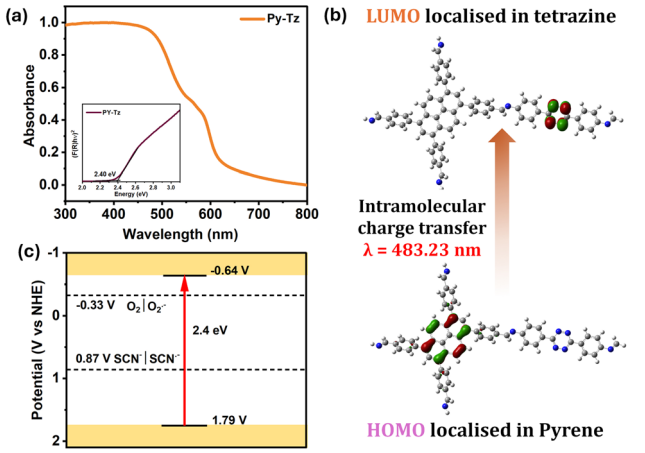

Fig. 2 (a) Solid-state UV-vis spectra and Tauc plot of **Py-Tz** COF (inset). (b) Electronic distribution of HOMO–LUMO of **Py-Tz** COF obtained from DFT calculation. (c) Schematic band diagram of **Py-Tz** COF indicating the valence band and conductance band position with respect to E_0 ($O_2|O_2^{\bullet-}$) and E_0 ($SCN^-|SCN^{\bullet-}$).

negative than the reduction potential of oxygen (O_2) to the superoxide radical anion ($O_2^{\bullet-}$) ($E_0 = -0.33$ V *vs.* NHE), while the VB is more positive than the potential of SCN^- to $SCN^{\bullet-}$ ($E_0 = 0.87$ V *vs.* NHE) (Fig. 2c).[44,45] This indicates **Py-Tz** COF can efficaciously reduce O_2 to $O_2^{\bullet-}$ and oxidize SCN^- to $SCN^{\bullet-}$ under visible light irradiation. Photogenerated separation and recombination of charges was assessed through transient photocurrent measurements, revealing minimal current in the absence of light, which significantly increased upon illumination (Fig. S14c). Additionally, electrochemical impedance spectroscopy (EIS) was conducted under both illuminated and dark conditions revealing a reduced semicircle radius in the Nyquist plot under light indicating a lower charge transfer resistance (Fig. S14b). Together, these results demonstrate efficient electron–hole separation in the **Py-Tz** COF upon light exposure. Moreover, electron paramagnetic resonance was also measured in the presence of light in order to evaluate the ability of **Py-Tz** COF to generate unpaired electrons. The gradual increase in EPR signal over time strongly indicated the generation and accumulation of photoexcited electron–hole pairs on the COF framework (Fig. S15).[46–49]

To get insight into the distinct contributions of photogenerated electrons and holes to drive photocatalytic reactions, two reactions were performed separately: electron-driven hydroxylation and hole-driven thiocyanation reaction. At first, the photocatalytic hydroxylation reaction was conducted with 4-formylphenylboronic acid (**1a**) (0.125 mmol) as the model substrate and acetonitrile (5 mL) as the solvent. The reaction was carried out in the presence of oxygen (O_2) as the oxidant and triethylamine (TEA) (0.43 M) as the sacrificial electron donor (Table 1; Entry 1). The successful formation of the product was confirmed by the ^{1}H NMR study (Fig. S16). The yield of the product was also obtained from the NMR, which showed an impressive ≈99% yield of **1a** after 12 h of continuous visible light irradiation. Control experiments were performed without

Table 1 Control experiments on hydroxylation reaction

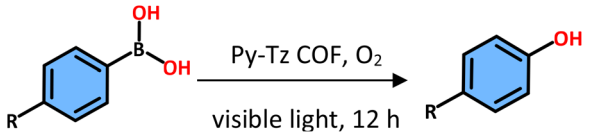

Entry	Variation of reaction condition	Yield[a] (%)
1	No variation	99%
2	Without photocatalyst	Not observed
3	Without light	Not observed
4	Without TEA	Not observed
5	Ar instead of O_2	Trace
6	Presence of $AgNO_3$	10%
7	Presence of *p*-benzoquinone	10%
8	Presence of L-histidine	97%

[a] Yield was calculated from ^{1}H NMR using 1,3,5-trimethoxybenzene as the internal standard. (1) Reaction condition: 0.125 mmol of boronic acid derivatives, 5 mL of CH_3CN solvent, triethylamine (TEA) (0.43 M), 2 mg catalyst, O_2 as oxidant, 12 h under irradiation of 300 W Xe lamp.

the photocatalyst, light, or TEA, which resulted in negligible product formation, highlighting the essential role of each component during the photocatalytic process (Table 1; Entries 2–4). Additionally, only trace amounts of product were observed under argon atmosphere, confirming that O_2 served as the primary oxidant in this catalysis (Table 1; Entry 5). The reaction yield was further quenched in the presence of $AgNO_3$ and *p*-benzoquinone as scavengers for electrons and superoxide radical anions ($O_2^{\bullet-}$), respectively, indicating active participation of these species in the photocatalytic process (Table 1; Entry 6 and 7). The nearly unchanged yield in the presence of L-histidine, a well-known singlet oxygen ($^1O_2$) scavenger, indicates negligible formation of $^1O_2$ in the reaction medium (Table 1; Entry 8). Additionally, various boronic acid derivatives with different functionalities (–CHO, $-CO_2H$, $-CO_2CH_3$, –Br, and –CN) were tested under optimized reaction conditions to demonstrate the broad applicability of this synthetic protocol. All substrates, regardless of the functional group, were effectively transformed into the intended products with excellent yields of ≈95–99%, demonstrating the effectiveness of **Py-Tz** COF as a photocatalyst for hydroxylation reactions (Table 2).

Table 2 Substrate scope of hydroxylation reaction

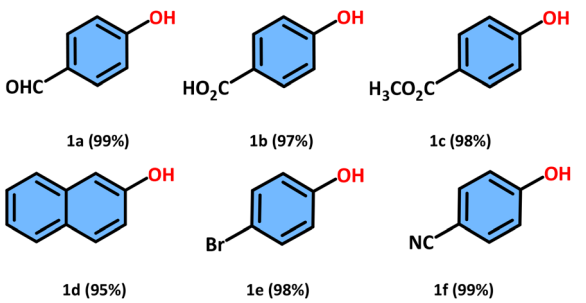

Table 3 Control experiments on thiocyanation reaction

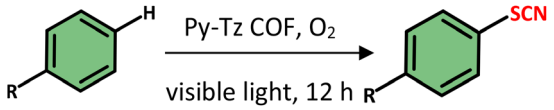

Entry	Variation of reaction condition	Yield[a] (%)
1	No variation	96%
2	Without photocatalyst	Not observed
3	Without light	Not observed
4	Ar instead of O_2	Trace
5	Presence of TEMPO	Trace
6	Presence of *p*-benzoquinone	14%
7	Presence of L-histidine	93%
8	CO_2 instead of O_2	74%

[a] Yield was calculated from ^{1}H NMR using 1,3,5-trimethoxybenzene as internal standard. (1) Reaction condition: 1.5 mmol of NH_4SCN, 0.5 mmol of the substrate, 5 mL of THF solvent, 2 mg catalyst, O_2 as oxidant, 12 h under irradiation of 300 W Xe lamp.

Next, we performed a hole-driven thiocyanation reaction by **Py-Tz** COF on aromatic compounds. To optimize the reaction conditions, *N*,*N*-dimethylaniline was selected as the model substrate (0.5 mmol), ammonium thiocyanate (NH_4SCN) (1.5 mmol) was used as the thiocyanate source, and THF was chosen as the solvent (5 mL) (Table 3; Entry 1). The formation of the desired product was confirmed by ^{1}H NMR study (Fig. S17). Further, several control studies suggested the indispensable role of photocatalyst, light, and O_2 during the catalysis (Table 3; Entry 2–4). Moreover, in the presence of a radical scavenger, such as TEMPO, only trace amounts of the product were detected, indicating that radicals are the primary active species, driving the photoredox reaction (Table 3; Entry 5). The addition of *p*-benzoquinone led to a significant decrease in the reaction yield to ≈14%, indicating that superoxide radicals ($O_2^{\bullet-}$) are the predominant reactive species (Table 3; Entry 6). In contrast, the thiocyanation reaction proceeded efficiently in the presence of L-histidine, suggesting that singlet oxygen ($^1O_2$) does not play a significant role in the reaction pathway (Table 3; Entry 7).[50] After establishing the feasibility of the reaction under standard conditions, various aniline derivatives were investigated as substrates. Notably, the substrates containing tertiary amine nitrogen atoms (Table 4) were successfully transformed into the 4-thiocyanated products (Table 4, **2a**–**2d**) with high chemoselectivity and yield (≈91–98%), regardless of the substituents on the nitrogen atom. Further, secondary amines (**2e** and **2f**) were also explored, including heterocycle indole, resulting in the formation of C-3 thiocyanation products with good yield (≈89%). To assess the benefits of the heterogeneous nature of COF as a photocatalyst, we conducted a recyclability test over four consecutive cycles (Fig. S18). After each catalytic reaction, COF samples were recovered through centrifugation, washed with THF and ethanol, dried at 60 °C, and then used for the next cycle. The **Py-Tz** COF exhibited outstanding recyclability, maintaining consistent yields in each cycle, without notable changes in PXRD, FTIR, FESEM, and TEM analyses (Fig. S19–S21).

Table 4 Substrate scope of thiocyanation reaction

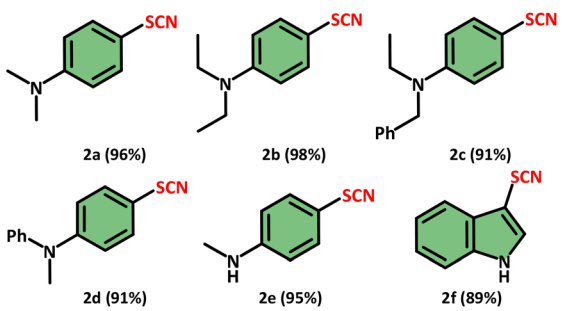

To investigate the underlying reaction mechanism, a steady-state photoluminescence quenching experiment was conducted. The broad emission of **Py-Tz** COF, centered at 480 nm in acetonitrile dispersion, was significantly quenched in an O_2-rich atmosphere (Fig. S22a). Time-correlated single photon counting (TCSPC) studies further revealed a reduced lifetime under O_2-rich conditions of 1.75 ns compared to the argon atmosphere (2.56 ns) (Fig. S22b). These further demonstrate that, following photoexcitation, rapid electron transfer occurs from **Py-Tz** COF to O_2, leading to the generation of superoxide ($O_2^{\bullet-}$).[51] To detect key reactive oxygen species, a UV-vis experiment was conducted using *N*,*N*,*N*′,*N*′-tetramethyl-*p*-phenylenediamine (TMPD) in the presence of **Py-Tz** COF, O_2, and light. A noticeable increase in absorbance with prominent bands at 516 nm, 560 nm, and 615 nm indicated the formation of the cation–anion adduct between ($O_2^{\bullet-}$) and $TMPD^{\bullet+}$ cationic radical (Fig. 3a). Additionally, EPR spectroscopy was performed with 5,5-dimethyl-1-pyrroline-*N*-oxide (DMPO) for both hydroxylation and thiocyanation reactions. The strong EPR signal observed under light confirmed the formation of the DMPO-$O_2^{\bullet-}$ adduct, reinforcing that superoxide ($O_2^{\bullet-}$) was generated through a single electron transfer (SET) process (Fig. 3b and S23).[52] In addition, steady-state photoluminescence (PL) quenching was performed with varying concentrations of *N*,*N*-dimethylaniline. It was observed that as the concentration of *N*,*N*-dimethylaniline increased, the PL intensity was significantly quenched (Fig. 3c).[53] The Stern–Volmer constant and electron transfer rate were determined to be 54.32 M^{-1} and 2.12 $\times$ 10^{10} M^{-1} S^{-1}, respectively (Fig. S24a, b and Table S1). These data indicate that in the presence of amines, the photoexcited **Py-Tz** COF undergoes reductive quenching, forming the radical cation of the respective amines. To further reveal the progress of the reaction process and trap the reactive intermediates during the hydroxylation reaction *in situ* DRIFTS spectroscopy was performed under visible light irradiation and continuous O_2 purging conditions. After considering the substrate, triethyl amine, **Py-Tz** COF, and O_2, one background spectrum was collected before visible light irradiation. After visible light irradiation, various peaks were observed in the spectrum to identify the reactive species involved in this reaction. The peaks at 862 cm^{-1} and 952 cm^{-1} were attributed to O–O stretching frequencies.[54] Notably, the peaks at 1335 cm^{-1} and 1141 cm^{-1}

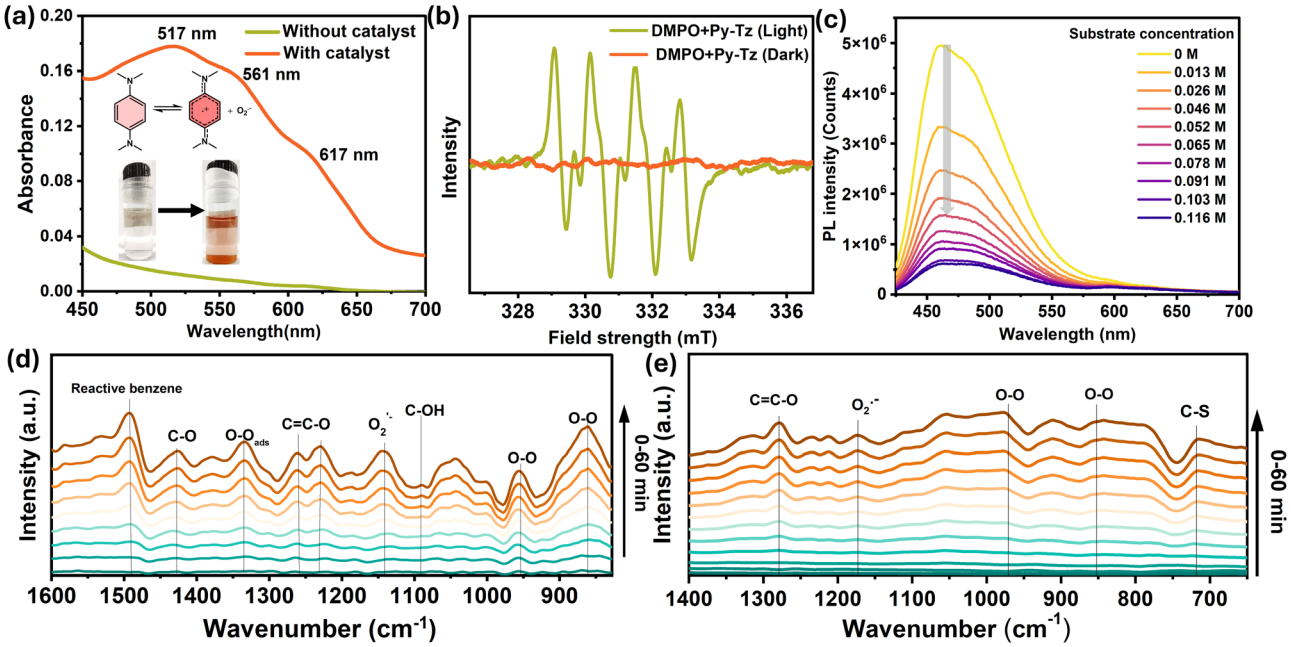

Fig. 3 (a) UV-vis spectra of TMPD radical cation formed by **Py-Tz** COF in the presence of light and O_2. (b) EPR spectra of DMPO-$O_2^{\cdot-}$ formed by **Py-Tz** COF in the presence of light. (c) Photoluminescence quenching experiment of **Py-Tz** COF in THF dispersion by varying concentrations of *N*,*N*-dimethylaniline. *In situ* DRIFT studies demonstrate the appearance of new peaks, showing the progression of (d) hydroxylation reaction and (e) thiocyanation reaction.

were assigned to the O–O vibration of adsorbed oxygen species (O–O_{ads}) and also suggesting initial adsorption of O_2 on the catalyst surface in mainly Yeager type.[55–57] The peak at 1143 cm^{-1} suggested adsorbed O_2 was reduced to $O_2^{\cdot-}$.[58] Notably, the stretching frequencies for C–O, C=C–O, and C–O–H were observed at 1427 cm^{-1}, 1261 cm^{-1}, and 1090 cm^{-1}, respectively (Fig. 3d), indicating the advancement of the hydroxylation reaction.[59–61] Similarly, *in situ* DRIFT experiment was also performed for the thiocyanation reaction in the presence of NH_4SCN, **Py-Tz** COF, O_2 and substrate. Similarly, the peaks associated with previously identified intermediates, such as O–O_{ads}, $O_2^{\cdot-}$, and O–O, were observed, along with a newly appeared peak at 711 cm^{-1}, suggesting the formation of the C–S bond (Fig. 3e).[62,63]

Furthermore, we conducted the photocatalytic reduction of CO_2 in the presence of *N*,*N*-dimethylaniline and NH_4SCN, aiming to elucidate the mechanistic pathway wherein the photoexcited **Py-Tz** COF facilitates electron transfer from its conduction band to CO_2, leading to CO generation. Simultaneously, the photogenerated holes are expected to drive the thiocyanation of *N*,*N*-dimethylaniline (Fig. S25a). The experiment was conducted in a THF medium under a CO_2 atmosphere, employing *N*,*N*-dimethylaniline (0.5 mmol) and NH_4SCN (1.5 mmol) as the sacrificial electron donor and substrates for the thiocyanation reaction (Table 3, Entry 8).[33] The photoreduced gaseous product was quantified using gas chromatography-mass spectrometry (GC-MS) analysis of the gas collected from the reactor headspace. After 12 hours of continuous irradiation, 690.2 μmol g^{-1} of CO was produced, while *N*,*N*-dimethyl-4-thiocyanatoaniline was obtained with a yield of ≈74% (Fig. S25b). Along with CO, a negligible amount of H_2 was also produced. An isotope labelling experiment conducted with $^{13}CO_2$ led to the formation of ^{13}CO, providing definitive evidence that the generated CO originates from CO_2 (Fig. S26c). Notably, *in situ* DRIFTS measurements of the thiocyanation reaction coupled with photocatalytic CO_2 reduction revealed a gradual emergence of multiple peaks within the 1000–2100 cm^{-1} range, indicating the sequential formation of various reaction intermediates responsible for CO_2 reduction process (Fig. S27). The infrared peak observed at 1526 cm^{-1} was attributed to the COOH* intermediate, a pivotal species in the transformation of CO_2 to CO.[25,33,64] Additionally, the observed peaks at 1707 cm^{-1} (CO bending mode), 1645 cm^{-1} ($CO_2^{\cdot-}$), and 2042 cm^{-1} (*CO), along with the characteristic vibrational signatures at 1378 cm^{-1} attributed to *m*-CO_3^{2-} species, indicate the successful formation of CO, providing strong evidence for the progression of the CO_2 reduction process.[65,66] Additionally, the peak observed at 731 cm^{-1} further confirmed the formation of the C–S bond during the thiocyanation reaction (Fig. S23). Thus, the simultaneous utilization of the electron–hole pair was demonstrated through the CO_2 reduction reaction (CO_2RR) and the thiocyanation reaction.

Further, in order to fully harness the photogenerated charge carriers (e^- and h^+) within a single photocatalytic system, we carried out both the hydroxylation of boronic acid and the thiocyanation of aniline derivatives in a one-pot reaction, in presence of 4-formylphenylboronic acid (0.125 mmol), NH_4SCN (1.5 mmol), *N*,*N*-diethylaniline (0.5 mmol), **Py-Tz** COF, O_2 and the reaction was performed in THF medium (Fig. 4a). The successful conversion of both substrates into the desired

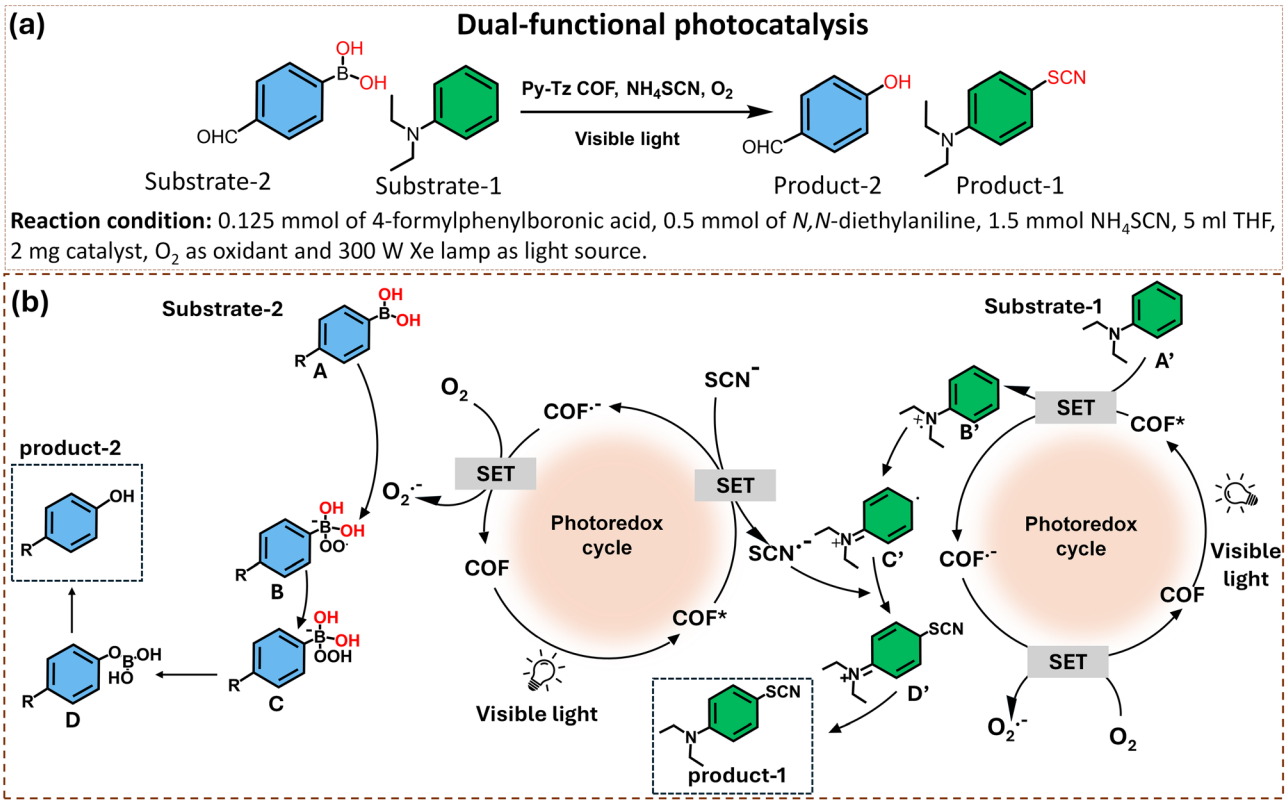

Fig. 4 (a) Reaction conditions and (b) plausible mechanism of dual-functional photocatalysis mediated by Py-Tz COF.

product was confirmed through NMR analysis ($Yield_{hydroxylation}$ ≈ 99% and $Yield_{thiocyanation}$ ≈46%) (Fig. S28). This dual-substrate transformation was enabled by the spatial separation of the HOMO on the pyrene unit and the LUMO on the tetrazine moiety within the COF framework (Fig. 2b). It is proposed that, upon visible light irradiation, intramolecular charge transfer (ICT) from the pyrene to the tetrazine results in the transfer of photoexcited electrons to the tetrazine moiety. These electrons activate the oxygen molecule *via* a single electron transfer (SET) process, leading to the formation of reactive superoxide radical anion ($O_2^{\bullet-}$). This $O_2^{\bullet-}$ radical anion, characterized by its Lewis basic nature, was captured by the boron atom of the boronic acids (A), leading to the formation of intermediate B. Subsequently, intermediate B is subjected to intermolecular proton abstraction, resulting in intermediate C. Following this, intermediate C participated in intramolecular aryl group migration, during which the aryl group attacked the oxygen atom and broke the weak O–O bond with the release of the OH^- group, leading to the formation of intermediate D. Finally, product-2 was produced from intermediate D through the hydrolysis process. At the same time, the photogenerated hole oxidized the aniline substrate (A′) and SCN^- leading to the formation of the corresponding anilinium radical cation (B′) and $SCN^{\bullet-}$ radical anion. The generated aniline radical cation (B′) transformed into its resonance structure (C′), which was attacked by $SCN^{\bullet-}$ radical to form an intermediate (D′). Subsequently, the intermediate D′ lost one proton to rearomatize and give the final product-1 (Fig. 4b).[67,68]

Conclusions

In summary, this study presents a unique strategy for dual-functional photoredox catalysis by a highly crystalline, porous, donor–acceptor-based COF. Following comprehensive physical, optical, and electrochemical characterization, **Py-Tz** COF was explored as a metal-free photocatalyst for the hydroxylation of boronic acids and C–H thiocyanation of anilines. The perfect donor–acceptor dyad formation, broad visible light absorbance, high surface area, and low exciton binding energy of **Py-Tz** contributed to the very high photoconversion efficiency of diverse substrates containing a wide range of functional groups. Finally, after elucidating the reaction mechanisms, **Py-Tz** was further investigated for the simultaneous photoconversion of boronic acids and aniline derivatives by utilizing e^- and h^+ simultaneously in a single pot. The distinct separation of the HOMO and LUMO within the COF framework enabled these electron- and hole-driven reactions to occur in parallel. Overall, this study introduces a unique approach for leveraging metal-free donor–acceptor based COFs in the dual-photoconversion of organic substrates, maximizing visible light utilization and minimizing waste product formation.

Author contributions

T. K. M., A. D., and T. M. designed the concept of this work. T. M., A. D. and D. M. performed major experiments and data analysis. T. K. M. assisted in the data analysis. T. M., A. D., and

T. K. M. were involved in the writing and editing of the manuscript. All authors contributed to the preparation of the manuscript.

Conflicts of interest

There are no conflicts to declare.

Data availability

All data supporting this article have been included either in the main manuscript or supplementary information (SI). The SI contains a detailed experimental section, synthesis, and additional data that support the findings of this study. Supplementary information is available. See DOI: **https://doi.org/10.1039/d5sc02909k**.

Acknowledgements

T. M. and A. D. acknowledge JNCASR for the fellowship. D. M. acknowledges UGC for the fellowship. T. K. M. gratefully acknowledges the Science and Engineering Research Board (SERB), Department of Science and Technology (DST) (projects SPR/2021/000592) and JNCASR for financial support. The SAMat research facility, Sheikh Saqr Laboratory (SSL) and Sheikh Saqr senior fellowship are also gratefully acknowledged.

References

1 A. Savateev and M. Antonietti, *ACS Catal.*, 2018, **8**, 9790–9808.
2 C. Dai and B. Liu, *Energy Environ. Sci.*, 2020, **13**, 24–52.
3 S. Kampouri and K. C. Stylianou, *ACS Catal.*, 2019, **9**, 4247–4270.
4 F. Niu, W. Tu, Y. Zhou, R. Xu and Z. Zou, *EnergyChem*, 2023, **5**, 100112.
5 T. Hisatomi, J. Kubota and K. Domen, *Chem. Soc. Rev.*, 2014, **43**, 7520–7535.
6 M.-Q. Yang, L. Shen, Y. Lu, S. W. Chee, X. Lu, X. Chi, Z. Chen, Q.-H. Xu, U. Mirsaidov and G. W. Ho, *Angew. Chem., Int. Ed.*, 2019, **58**, 3077–3081.
7 H. Lu, J. Zhao, L. Li, L. Gong, J. Zheng, L. Zhang, Z. Wang, J. Zhang and Z. Zhu, *Energy Environ. Sci.*, 2011, **4**, 3384–3388.
8 H. Liu, C. Xu, D. Li and H.-L. Jiang, *Angew. Chem., Int. Ed.*, 2018, **57**, 5379–5383.
9 Z. Jiao, Z. Zhai, X. Guo and X.-Y. Guo, *J. Phys. Chem. C*, 2015, **119**, 3238–3243.
10 X. Dai, M. Xie, S. Meng, X. Fu and S. Chen, *Appl. Catal., B*, 2014, **158–159**, 382–390.
11 B. Weng, Q. Quan and Y.-J. Xu, *J. Mater. Chem. A*, 2016, **4**, 18366–18377.
12 M. Wang, L. Li, J. Lu, N. Luo, X. Zhang and F. Wang, *Green Chem.*, 2017, **19**, 5172–5177.
13 H.-F. Ye, R. Shi, X. Yang, W.-F. Fu and Y. Chen, *Appl. Catal., B*, 2018, **233**, 70–79.
14 H. Wang, H. Wang, Z. Wang, L. Tang, G. Zeng, P. Xu, M. Chen, T. Xiong, C. Zhou, X. Li, D. Huang, Y. Zhu, Z. Wang and J. Tang, *Chem. Soc. Rev.*, 2020, **49**, 4135–4165.
15 X. Kang, X. Wu, X. Han, C. Yuan, Y. Liu and Y. Cui, *Chem. Sci.*, 2020, **11**, 1494–1502.
16 S. Liu, M. Tian, X. Bu, H. Tian and X. Yang, *Chem.–Eur. J.*, 2021, **27**, 7738–7744.
17 R. Chen, J.-L. Shi, Y. Ma, G. Lin, X. Lang and C. Wang, *Angew. Chem., Int. Ed.*, 2019, **58**, 6430–6434.
18 Y. Fan, D. W. Kang, S. Labalme, J. Li and W. Lin, *Angew. Chem., Int. Ed.*, 2023, **62**, e202218908.
19 Z. Liu, Z. Chen, H. Tong, M. Ji and W. Chu, *Green Chem.*, 2023, **25**, 5195–5205.
20 S. Trenker, L. Grunenberg, T. Banerjee, G. Savasci, L. M. Poller, K. I. M. Muggli, F. Haase, C. Ochsenfeld and B. V Lotsch, *Chem. Sci.*, 2021, **12**, 15143–15150.
21 J. Sun, H. Sekhar Jena, C. Krishnaraj, K. Singh Rawat, S. Abednatanzi, J. Chakraborty, A. Laemont, W. Liu, H. Chen, Y.-Y. Liu, K. Leus, H. Vrielinck, V. Van Speybroeck and P. Van Der Voort, *Angew. Chem., Int. Ed.*, 2023, **62**, e202216719.
22 W. Zhao, P. Yan, B. Li, M. Bahri, L. Liu, X. Zhou, R. Clowes, N. D. Browning, Y. Wu, J. W. Ward and A. I. Cooper, *J. Am. Chem. Soc.*, 2022, **144**, 9902–9909.
23 P. Das, J. Roeser and A. Thomas, *Angew. Chem., Int. Ed.*, 2023, **62**, e202304349.
24 W. Wang, W. Gao, X. Nie, W. Liu, X. Cheng, N. Shang, S. Gao and C. Wang, *J. Colloid Interface Sci.*, 2022, **616**, 1–11.
25 A. Dey, F. A. Rahimi, S. Barman, A. Hazra and T. K. Maji, *J. Mater. Chem. A*, 2023, **11**, 13615–13622.
26 Z. Li, T. Deng, S. Ma, Z. Zhang, G. Wu, J. Wang, Q. Li, H. Xia, S.-W. Yang and X. Liu, *J. Am. Chem. Soc.*, 2023, **145**, 8364–8374.
27 G.-B. Wang, F.-C. Zhu, Q.-Q. Lin, J.-L. Kan, K.-H. Xie, S. Li, Y. Geng and Y.-B. Dong, *Chem. Commun.*, 2021, **57**, 4464–4467.
28 S. Quideau, D. Deffieux, C. Douat-Casassus and L. Pouységu, *Angew. Chem., Int. Ed.*, 2011, **50**, 586–621.
29 V. Elumalai and J. H. Hansen, *RSC Adv.*, 2020, **10**, 40582–40587.
30 D. Wu, Y. Duan, K. Liang, H. Yin and F.-X. Chen, *Chem. Commun.*, 2021, **57**, 9938–9941.
31 X. Duan, X. Liu, X. Cuan, L. Wang, K. Liu, H. Zhou, X. Chen, H. Li and J. Wang, *J. Org. Chem.*, 2019, **84**, 12366–12376.
32 E. de Oliveira Lima Filho and I. Malvestiti, *ACS Omega*, 2020, **5**, 33329–33339.
33 A. Dey, J. Pradhan, S. Biswas, F. Ahamed Rahimi, K. Biswas and T. K. Maji, *Angew. Chem., Int. Ed.*, 2024, **63**, e202315596.
34 S. Biswas, A. Dey, F. A. Rahimi, S. Barman and T. K. Maji, *ACS Catal.*, 2023, **13**, 5926–5937.
35 W. Li, X. Huang, T. Zeng, Y. A. Liu, W. Hu, H. Yang, Y.-B. Zhang and K. Wen, *Angew. Chem., Int. Ed.*, 2021, **60**, 1869–1874.
36 W. Chen, Z. Yang, Z. Xie, Y. Li, X. Yu, F. Lu and L. Chen, *J. Mater. Chem. A*, 2019, **7**, 998–1004.
37 M. Plugge, V. Alain-Rizzo, P. Audebert and A. M. Brouwer, *J. Photochem. Photobiol., A*, 2012, **234**, 12–20.

38 D. G. Lidzey, D. D. C. Bradley, A. Armitage, S. Walker and M. S. Skolnick, *Science*, 2000, **288**, 1620–1623.
39 S. Melissen, T. Le Bahers, S. N. Steinmann and P. Sautet, *J. Phys. Chem. C*, 2015, **119**, 25188–25196.
40 W. Zhang, Z. Deng, J. Deng, C.-T. Au, Y. Liao, H. Yang and Q. Liu, *J. Mater. Chem. A*, 2022, **10**, 22419–22427.
41 Z.-A. Lan, G. Zhang, X. Chen, Y. Zhang, K. A. I. Zhang and X. Wang, *Angew. Chem., Int. Ed.*, 2019, **58**, 10236–10240.
42 S. Sun, T. Salim, N. Mathews, M. Duchamp, C. Boothroyd, G. Xing, T. C. Sum and Y. M. Lam, *Energy Environ. Sci.*, 2014, **7**, 399–407.
43 X. Yu, S. Tian, F. Zhang, G. Gao, C. Zhang, Y. Han, S. Ji, H. Guo and X.-H. Jin, *ACS Sustain. Chem. Eng.*, 2022, **10**, 16182–16188.
44 M. Hosseini-Sarvari, Z. Hosseinpour and M. Koohgard, *New J. Chem.*, 2018, **42**, 19237–19244.
45 J. Liu, C. Tuo, W.-Y. Xiao, M.-Y. Qi, Y. Yusran, Z. Wang, H. Li, C. Guo, J. Song, S. Qiu, Y.-J. Xu and Q. Fang, *Angew. Chem., Int. Ed.*, 2025, **64**, e202416240.
46 X. Dong, F. Zhang, Y. Wang, F. Huang and X. Lang, *Appl. Catal., B*, 2024, **345**, 123660.
47 N. Liu, S. Xie, Y. Huang, J. Lu, H. Shi, S. Xu, G. Zhang and X. Chen, *Adv. Energy Mater.*, 2024, **14**, 2402395.
48 H. Qiao, L. Yang, X. Yang, J. Wang, Y. Chen, L. Zhang, W. Sun, L. Zhai and L. Mi, *Chem.–Eur. J.*, 2022, **28**, e202200600.
49 E. Jin, M. Asada, Q. Xu, S. Dalapati, M. A. Addicoat, M. A. Brady, H. Xu, T. Nakamura, T. Heine, Q. Chen and D. Jiang, *Science*, 2017, **357**, 673–676.
50 K. Verma, Mohit and K. R. J. Thomas, *Langmuir*, 2024, **40**, 24148–24161.
51 G. Li, T. Qiu, Q. Wu, Z. Zhao, L. Wang, Y. Li, Y. Geng and H. Tan, *Angew. Chem., Int. Ed.*, 2024, **63**, e202405396.
52 M.-Y. Yang, S.-B. Zhang, M. Zhang, Z.-H. Li, Y.-F. Liu, X. Liao, M. Lu, S.-L. Li and Y.-Q. Lan, *J. Am. Chem. Soc.*, 2024, **146**, 3396–3404.
53 A. Dey, S. Chakraborty, A. Singh, F. A. Rahimi, S. Biswas, T. Mandal and T. K. Maji, *Angew. Chem., Int. Ed.*, 2024, **63**, e202403093.
54 M. Kou, Y. Wang, Y. Xu, L. Ye, Y. Huang, B. Jia, H. Li, J. Ren, Y. Deng, J. Chen, Y. Zhou, K. Lei, L. Wang, W. Liu, H. Huang and T. Ma, *Angew. Chem., Int. Ed.*, 2022, **61**, e202200413.
55 Y. Hou, P. Zhou, F. Liu, Y. Lu, H. Tan, Z. Li, M. Tong and J. Ni, *Angew. Chem., Int. Ed.*, 2024, **63**, e202318562.
56 Y. Luo, B. Zhang, C. Liu, D. Xia, X. Ou, Y. Cai, Y. Zhou, J. Jiang and B. Han, *Angew. Chem., Int. Ed.*, 2023, e202305355.
57 Z. Teng, Q. Zhang, H. Yang, K. Kato, W. Yang, Y.-R. Lu, S. Liu, C. Wang, A. Yamakata, C. Su, B. Liu and T. Ohno, *Nat. Catal.*, 2021, **4**, 374–384.
58 C. Chu, D. Yao, Z. Chen, X. Liu, Q. Huang, Q. Li and S. Mao, *Small*, 2023, **19**, 2303796.
59 R. Schulte-Ladbeck, A. Edelmann, G. Quintás, B. Lendl and U. Karst, *Anal. Chem.*, 2006, **78**, 8150–8155.
60 L. C. Pacheco-Londoño, J. R. Castro-Suarez and S. P. Hernández-Rivera, *Adv. Opt. Technol.*, 2013, **2013**, 532670.
61 F. Liu, P. Zhou, Y. Hou, H. Tan, Y. Liang, J. Liang, Q. Zhang, S. Guo, M. Tong and J. Ni, *Nat. Commun.*, 2023, **14**, 4344.
62 L. Wang, J. Liu, H. Wang, H. Cheng, X. Wu, Q. Zhang and H. Xu, *Sci. Bull.*, 2021, **66**, 265–274.
63 S. Li, L. Hu, Z. Qian, J. Yin, J. Tang, C. Pan, G. Yu and K. A. I. Zhang, *ACS Catal.*, 2023, **13**, 12041–12047.
64 R. Zhang, H. Wang, S. Tang, C. Liu, F. Dong, H. Yue and B. Liang, *ACS Catal.*, 2018, **8**, 9280–9286.
65 X. Li, Y. Sun, J. Xu, Y. Shao, J. Wu, X. Xu, Y. Pan, H. Ju, J. Zhu and Y. Xie, *Nat. Energy*, 2019, **4**, 690–699.
66 S. Karmakar, S. Barman, F. A. Rahimi and T. K. Maji, *Energy Environ. Sci.*, 2021, **14**, 2429–2440.
67 B. Luo, Y. Zhang, Y. Chen and J. Huo, *Mater. Adv.*, 2022, **3**, 4699–4706.
68 P. Zhang, Y. Yin, Z. Wang, C. Yu, Y. Zhu, D. Yan, W. Liu and Y. Mai, *Macromolecules*, 2021, **54**, 3543–3553.